

Characterization and Evaluation of TiB_2 -AlN Composites for Armor Applications

by Tomoko Sano, Gary Gilde, and Jim Campbell

ARL-TR-6568

September 2013

NOTICES

Disclaimers

The findings in this report are not to be construed as an official Department of the Army position unless so designated by other authorized documents.

Citation of manufacturer's or trade names does not constitute an official endorsement or approval of the use thereof.

Destroy this report when it is no longer needed. Do not return it to the originator.

Army Research Laboratory

Aberdeen Proving Ground, MD 21005-5069

ARL-TR-6568**September 2013**

Characterization and Evaluation of TiB_2 -AlN Composites for Armor Applications

**Tomoko Sano, Gary Gilde, and Jim Campbell
Weapons and Materials Research Directorate, ARL**

Approved for public release; distribution is unlimited.

REPORT DOCUMENTATION PAGE			Form Approved OMB No. 0704-0188		
<p>Public reporting burden for this collection of information is estimated to average 1 hour per response, including the time for reviewing instructions, searching existing data sources, gathering and maintaining the data needed, and completing and reviewing the collection information. Send comments regarding this burden estimate or any other aspect of this collection of information, including suggestions for reducing the burden, to Department of Defense, Washington Headquarters Services, Directorate for Information Operations and Reports (0704-0188), 1215 Jefferson Davis Highway, Suite 1204, Arlington, VA 22202-4302. Respondents should be aware that notwithstanding any other provision of law, no person shall be subject to any penalty for failing to comply with a collection of information if it does not display a currently valid OMB control number.</p> <p>PLEASE DO NOT RETURN YOUR FORM TO THE ABOVE ADDRESS.</p>					
1. REPORT DATE (DD-MM-YYYY) September 2013		2. REPORT TYPE Final		3. DATES COVERED (From - To) June 2005—November 2008	
4. TITLE AND SUBTITLE Characterization and Evaluation of TiB ₂ -AlN Composites for Armor Applications			5a. CONTRACT NUMBER		
			5b. GRANT NUMBER		
			5c. PROGRAM ELEMENT NUMBER		
6. AUTHOR(S) Tomoko Sano, Gary Gilde, and Jim Campbell			5d. PROJECT NUMBER AH84		
			5e. TASK NUMBER		
			5f. WORK UNIT NUMBER		
7. PERFORMING ORGANIZATION NAME(S) AND ADDRESS(ES) U.S. Army Research Laboratory ATTN: RDRL-WMM-E Aberdeen Proving Ground, MD 21005-5069			8. PERFORMING ORGANIZATION REPORT NUMBER ARL-TR-6568		
9. SPONSORING/MONITORING AGENCY NAME(S) AND ADDRESS(ES)			10. SPONSOR/MONITOR'S ACRONYM(S)		
			11. SPONSOR/MONITOR'S REPORT NUMBER(S)		
12. DISTRIBUTION/AVAILABILITY STATEMENT Approved for public release; distribution is unlimited.					
13. SUPPLEMENTARY NOTES					
14. ABSTRACT <p>Seven composites with titanium diboride (TiB₂) and aluminum nitride (AlN) of varying compositions were consolidated by hot pressing. The compositions examined were 30-vol% TiB₂ / 70-vol% AlN, 50-vol% TiB₂ / 50-vol% AlN, and 70-vol% TiB₂ / 30-vol% AlN. One TiB₂ powder was used with three AlN powders: two with finer particle sizes and one with larger particle sizes. All the composites were consolidated to near full density. Microstructural, mechanical-property, and ballistic depth-of-penetration (DOP) evaluations were conducted. Theoretical phase calculations were used to determine and explain the formation of the detected impurities.</p> <p>The flexural strength and mass efficiency results from the four-point bend and DOP tests, respectively, showed that most of the composite compositions performed better than either monolithic TiB₂ or AlN material. The increase in fracture toughness from microcrack formation and crack bridging is believed to be the cause of the synergistic effects.</p>					
15. SUBJECT TERMS ceramic composite, TiB ₂ , AlN, microstructure, mechanical properties					
16. SECURITY CLASSIFICATION OF:			17. LIMITATION OF ABSTRACT	18. NUMBER OF PAGES	19a. NAME OF RESPONSIBLE PERSON Tomako Sano
a. REPORT Unclassified	b. ABSTRACT Unclassified	c. THIS PAGE Unclassified			19b. TELEPHONE NUMBER (Include area code) 410-306-0923

Contents

List of Figures	iv
List of Tables	v
Acknowledgments	vi
1. Introduction	1
2. Experimental	2
3. Phase Diagram Determination	3
4. Results	4
4.1 Powder Characterization	4
4.2 Composite Characterization	6
4.3 Mechanical Property Characterization	11
4.4 Residual Stress Characterization	13
4.5 Phase Diagram of $\text{TiB}_2\text{-AlN}$	13
4.6 Mass Efficiency Results	15
5. Discussion	16
6. Conclusions	19
7. References	20
Distribution List	23

List of Figures

Figure 1. XRD spectrum of TiB_2 powder.....	5
Figure 2. EDS spectrum of a BN particle.	5
Figure 3. XRD spectra of all three AlN powders. Spectra from top to bottom; Atofina AlN, Stark AT, and AlN Stark C.	6
Figure 4. SEM images of (a) 30-70 TiB_2 -AlN, (b) 50-50 TiB_2 -AlN, and (c) 70-30 TiB_2 -AlN.....	7
Figure 5. (a) Phase ID map of 50-50 TiB_2 -AlN (with the Atofina AlN) before EDS aided correction. Arrows point to grains with erroneously identified phases. White areas are pores or voids where grains were pulled out during the polishing step. Green grains are TiB_2 and red grains are AlN. (b) Corrected phase map where green grains are TiB_2 and blue grains are AlN. (c) EBSD inverse pole figure map of the same area. The standard stereographic triangle key indicates the orientation corresponding to the grain color.	8
Figure 6. (a) Inverse pole figure map to the surface parallel to hot-pressing direction and (b) surface perpendicular to the hot-pressing direction.	9
Figure 7. Inverse pole figure map of AlN.....	10
Figure 8. Number fraction of misorientation angles (a) for TiB_2 surfaces perpendicular to the hot pressing direction and TiB_2 surfaces parallel to the hot pressing direction compared to a random, non-textured case, and (b) for AlN surfaces compared to random.	10
Figure 9. Example of (a) 30-70 TiB_2 -AlN (with Atofina AlN) bend bar fracture surface with grain cluster flaw, circled above (flexural strength = 338.4 MPa) and (b) 50-50 TiB_2 -AlN (with Starck C AlN) bend bar fracture surface with undetermined flaw (flexural strength = 576.7 MPa).	12
Figure 10. Possible phases in the binary and ternary Ti-B-Al-N system.....	14
Figure 11. (a) Quaternary isothermal section at constant Ti atomic content, $X(\text{Ti})=0.1$, at $T = 1573 \text{ K}$ and (b) Quaternary isothermal section at constant B atomic content, $X(\text{B})=0.1$, at $T = 1573 \text{ K}$	14
Figure 12. (a) SEM image of 50-vol% TiB_2 / 50-vol% AlN (with Atofina AlN) showing what is believed to be AlN and γ -AlON decomposed eutectoid regions and (b) SEM image of 70-vol% TiB_2 / 30-vol% AlN (with Atofina AlN) showing possibly TiN impurities at the grain boundaries.....	15
Figure 13. Em vs. velocity for some of the composites and pure TiB_2 and pure AlN.	16
Figure 14. (a) Intergranular fracture surface of 50-50 TiB_2 -AlN with the coarse grained Stark AT AlN and (b) transgranular fracture surface of 50-50 TiB_2 -AlN with the fine grained Atophina AlN showing cleavage facets.	18

List of Tables

Table 1. Densities of the TiB_2 -AlN composites.	6
Table 2. Flexural strengths and Weibull modulus values.	11
Table 3. Knoop hardness values for surfaces perpendicular to the hot-pressing direction and parallel to the hot-pressing direction.....	12
Table 4. Elastic modulus, shear modulus, and Poisson's ratio for some of the composites.....	12
Table 5. Fracture toughness values.....	13

Acknowledgments

Special thanks and acknowledgements go to the following people who assisted and contributed to the data gathering of this work: Paul Huang, Ryan McCuiston, Herbert Miller, Matthew Motyka, and Thomas Juliano, all of whom are in the Weapons and Materials Research Directorate of the U.S. Army Research Laboratory.

1. Introduction

The need for lighter combat vehicles has driven the armor technology community to develop advanced ceramic materials for armor applications. Ceramics generally have lower densities than metals; however, ceramics are brittle materials that cannot sustain plastic strains and large collateral-damage results upon ballistic impact (1). Improving the brittle nature of ceramics is one of the key issues to overcome. Some have suggested a gradient material approach, or combining a material with high hardness and another with high ductility (2). With this suggestion in mind, a promising two-phase ceramic composite of titanium diboride (TiB_2) and aluminum nitride (AlN) was chosen to be evaluated.

TiB_2 has been reported (3) to have high strength, high melting point, high hardness, and a density of 4.50 g/cm^3 . Due to its properties, TiB_2 has been used in structural and wear applications, including armor, cutting tools, and wear-resistant coatings. TiB_2 belongs in the hexagonal space group $\text{P6}/\text{mm}$. The lattice constants typically range from $a = 3.0292 \text{ \AA}$ and $c = 3.2196 \text{ \AA}$ ($c/a = 1.063$) (4) to $a = 3.070 \text{ \AA}$ and $c = 3.262 \text{ \AA}$ ($c/a = 1.063$) (5), and the anisotropic coefficient of thermal expansion (CTE) at room temperature for the a axis ranges from $\alpha_a = 5.9 \times 10^{-6} \text{ K}^{-1}$ (6) to $6.4 \times 10^{-6} \text{ K}^{-1}$ (3), and for the c axis, $\alpha_c = 8.5 \times 10^{-6} \text{ K}^{-1}$ (6) to $9.2 \times 10^{-6} \text{ K}^{-1}$ (3).

AlN belongs in a hexagonal space group, $\text{P6}_3\text{mc}$, with lattice constants of $a = 3.1114 \text{ \AA}$ and $c = 4.9792 \text{ \AA}$ (7). AlN, which has a density of 3.26 g/cm^3 , is known for high thermal conductivity and electrical resistivity, and has unique mechanical properties as well. It was discovered to undergo a brittle to ductile transition at the confining pressure of 0.55 GPa (8, 9). AlN also has anisotropic CTE values. At room temperature for the a axis, the CTE is $\alpha_a = 5.3 \times 10^{-6} \text{ K}^{-1}$ and for the c axis, $\alpha_c = 4.2 \times 10^{-6} \text{ K}^{-1}$ (10). It is worth noting that unlike TiB_2 , AlN contracts more along the a axis than the c axis.

Other researchers have studied the processing, mechanical properties, and microstructural features of composites consisting of TiB_2 and AlN phases. These studies include composite synthesis by reactive sintering (11), microwave sintering (12), pressureless sintering (13), and hot pressing TiB_2 and using AlN as a sintering aid (14). The composite microstructure as well as mechanical properties such as hardness, flexural strength, fracture toughness, and Young's modulus have been investigated (11–16). In addition, Zdaniewski has identified structural defects and studied the fracture mechanisms (15, 16).

2. Experimental

One TiB_2 powder was used for this study. The TiB_2 powder (Stark D) was obtained from Stark. The TiB_2 particles were equiaxed and ranged from 3.0 to 6.0 μm in diameter. The equiaxed AlN powder (Atofina Pyrofine A) with particle size ranging from 0.5 to 0.80 μm was supplied by Atofina. Other AlN powders were also utilized to determine the effects of different particle morphologies on the ceramic composite microstructure and performance. The other powders were from Stark and included the Stark C AlN powder with the manufacturer's reported particle size range of 0.8–1.8 μm and the Stark AT AlN powder with particle size range of 7.0–11.0 μm . However, upon examination under the field emission gun scanning electron microscope (SEM), the Stark C AlN powder showed some elongated particles that were well over 3.0 μm in length. The Stark AT AlN powder also had several particles that were elongated in shape. All the powders were examined in the SEM and by x-ray diffraction (XRD).

Sets of powders making up 30-vol% TiB_2 / 70-vol% AlN (from now on referred to as 30-70 TiB_2 -AlN), 50-vol% TiB_2 / 50-vol% AlN (50-50 TiB_2 -AlN), and 70-vol% TiB_2 / 30-vol% AlN (70-30 TiB_2 -AlN) were ball milled with Al_2O_3 balls in acetone for 24 h. The mixed powders were then hot pressed at 2073 K (1800 °C) under 34.5 MPa of pressure for 3 h in argon. The 70-30 TiB_2 -AlN powders were hot pressed at 2173 K (1900 °C) under 20.68 MPa of pressure in argon for 3 h. Smaller samples from the relative middle of the hot pressed disk were obtained by cutting the 4- or 6-in-diameter disks with the Buehler Isomet4000 saw. The smaller samples were mounted with the Struers Isofast hot mount and polished on the Struers Rotopol 31 automatic polisher. The following polishing steps were used for all the samples:

1. A 15- μm diamond solution with Struers alcohol-based DP blue lubricant, 35-N force at 150 rpm.
2. A 9- μm diamond solution with Struers DP blue lubricant, 35-N force at 150 rpm.
3. A 3- μm diamond solution with Struers DP blue lubricant, 35-N force at 150 rpm on a resin-polishing surface.
4. A 3- μm diamond solution with Struers DP blue lubricant, 30-N force at 150 rpm on a silk-polishing surface.
5. A 1- μm diamond solution with Struers DP blue lubricant, 25-N force at 150 rpm.
6. A 1/4- μm diamond solution with Struers DP blue lubricant, 20-N force at 150 rpm.
7. Finish on the vibramet polisher with Struers OP-U 0.04- μm or Extec 0.02- μm colloidal silica solution.

After each polishing step, the samples were cleaned with ethanol, and after the final polishing step, the samples were ultrasonically cleaned with ethanol then DI water. The cleaned, polished samples were examined by SEM, energy dispersive spectroscopy (EDS), and electron backscattered diffraction (EBSD) to characterize the microstructure.

The 30-70 TiB₂-AlN sample hot pressed with the Atofina AlN; three sets of 50-50 TiB₂-AlN samples hot pressed with the Atofina, Stark AT, and the Stark C AlN powder; the 30-70 TiB₂-AlN sample hot pressed with the Atofina AlN powder, 100% TiB₂, and 100% AlN. All samples were machined into ASTM C 1161 (17) “B” bars to determine flexure strength by four-point bend tests. Knoop hardness values were also determined for these samples, using 2-Kg loads. The Knoop hardness values were measured on the surfaces perpendicular to, and surfaces parallel to the hot pressing direction to determine, if any, effects due to the hot pressing direction on the mechanical properties. The three sets of 50-50 TiB₂-AlN also were subjected to the ASTM 1421 (18) single-edge precracked beam method to determine the fracture toughness. Other properties were determined by ultrasonic velocity measurements, per ASTM E 494 (19). These include density, elastic modulus, shear modulus, Young’s modulus, and Poisson’s Ratio.

To determine the residual stress of the AlN, a 50-50 TiB₂-AlN sample hot pressed with the Atofina AlN was examined by Raman spectroscopy. TiB₂ is not Raman active, but AlN is. The Raman signal of the E₂ (high) phonon frequency was used to compare the pure AlN to the AlN in the 50-50 TiB₂-AlN composite. The Raman stress relation for bulk AlN has been determined by Kuball et al. (20) as 0.2 GPa/cm⁻¹. They also determined the unstressed pure AlN has E₂ phonon frequency of 656 cm⁻¹. A Raman shift in the E₂ phonon position for the composite’s spectra will indicate a compressive or tensile stress. Using the Raman stress factor, the quantity of residual stress was calculated. To validate the findings, theoretical calculations of the residual stress were also conducted.

The ballistic performances of these ceramic composites were determined by depth-of-penetration (DOP) tests. The DOP tests were performed on 4-in-diameter tiles of all 50-50 TiB₂-AlN compositions hot pressed with the three different AlN powders. In addition, 30-70 TiB₂-AlN hot pressed with Stark C AlN powder and 70-30 TiB₂-AlN hot pressed with Stark AT AlN powder were evaluated.

3. Phase Diagram Determination

In addition to the experimental work, phase-diagram calculations were conducted by Fabrichnaya and Seifert (21). The Ti-Al-B-N quaternary system was calculated to better predict the possible phases formed at relevant temperatures during processing and sintering steps. The required calculation for determining the phase diagrams were performed by the Thermo-Calc software. In this research, the liquid phase was described by the substitution model, excess

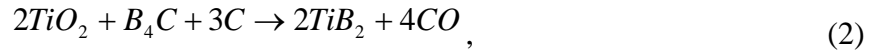
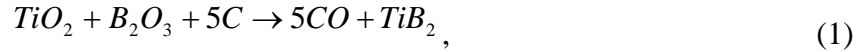
energy described by Redlich-Kister-Muggianu polynomial, the solid phases by the sublattice model expressed in the compound energy, and the gas phase was assumed to be ideal solution. The database for the quaternary Al-Ti-B-N system was created by combining the Al-Ti-N description with the Al-B, Ti-B and B-N binary systems. In addition, ternary diagrams of Al-B-Ti, Ti-Al-N, Ti-B-N, and Al-B-N were created at a variety of temperatures as a prerequisite for the quaternary system.

The two quaternary phase diagrams were calculated at 1572 K with constant one mole % Ti and one mole % B, respectively.

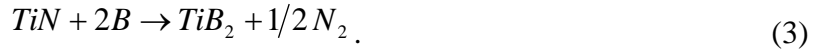
4. Results

4.1 Powder Characterization

The TiB_2 and AlN starting powders were examined by XRD, SEM, and EDS to determine the impurities and morphologies of the powders. The XRD patterns (see figure 1) for the TiB_2 powder used for all the samples showed not only TiB_2 peaks, but also TiN peaks. TiB_2 powder can be produced by carbothermal reduction (22, 23) of TiO_2 and boron compound as shown in the following reaction equations (1) and (2):



or a solid-state reaction of TiN with amorphous boron (24) as shown in reaction equation 3. The TiN would be the result of incomplete reaction of TiN, which was there either due to the reaction of titanium and nitrogen during carbothermal reduction in presence of nitrogen or TiN being used as a starting material.



The EDS spectrum also indicated the presence of BN (see figure 2). It is hypothesized that the amorphous boron that again was either there as a primary reactant or a partial step during carbothermal reduction in presence of nitrogen, reacted with the nitrogen to form BN. In the results section, phase-diagram calculations show that TiN and BN can be by-products of the Ti-B-Al-N system. The XRD patterns for the AlN powders were all comparable, showing only AlN peaks (figure 3). However, EDS analysis showed some oxygen, which could be surface contamination, and sulfur impurities.

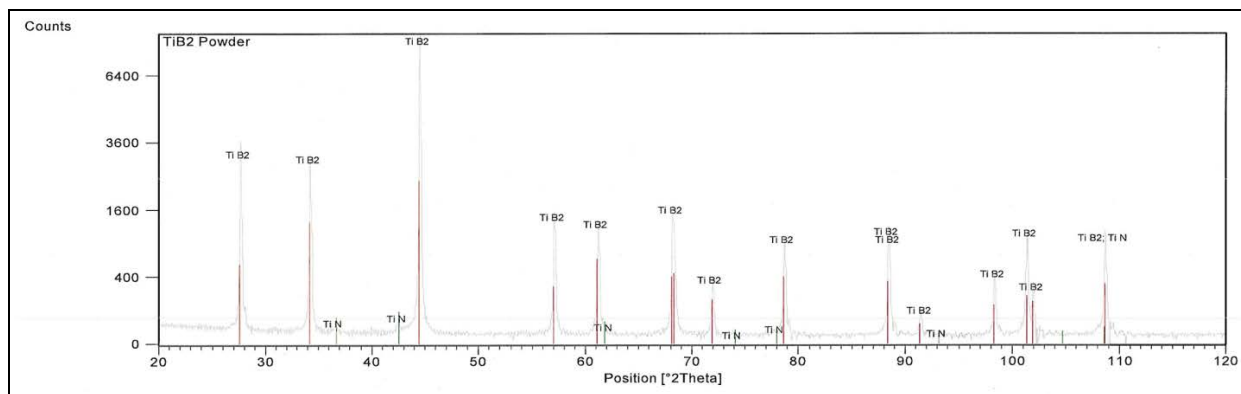


Figure 1. XRD spectrum of TiB₂ powder.

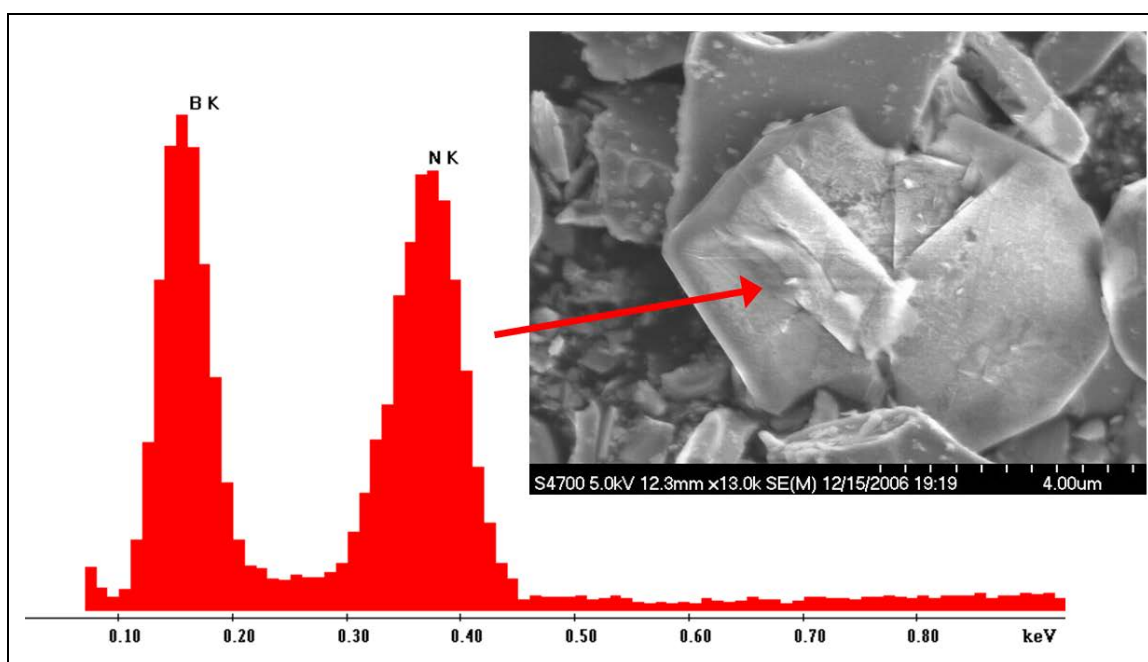


Figure 2. EDS spectrum of a BN particle.

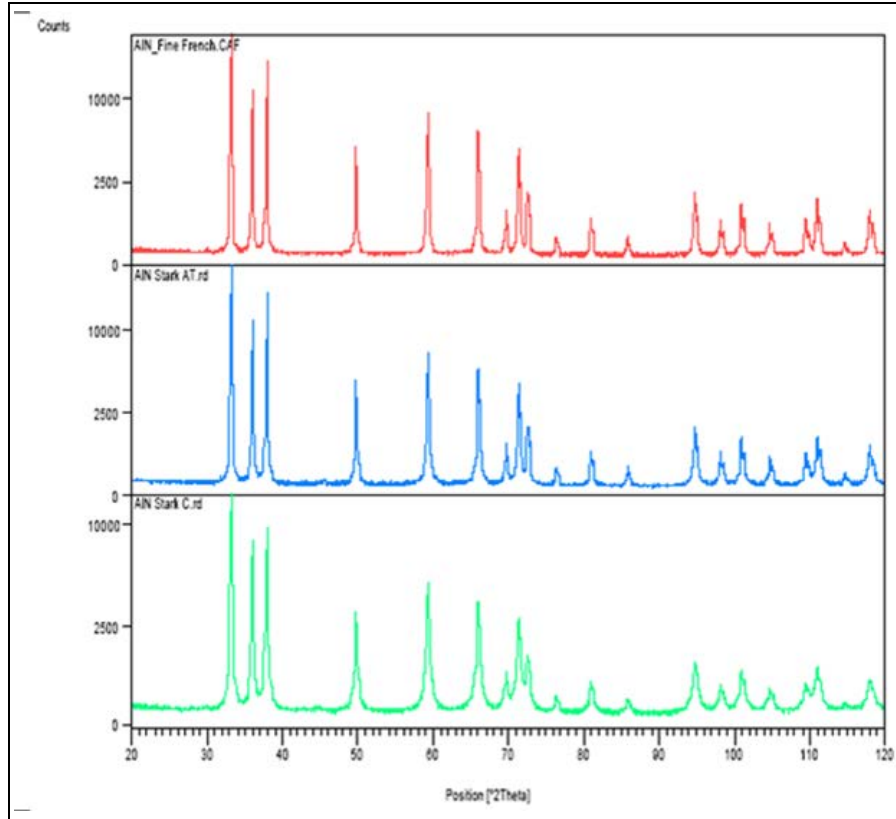


Figure 3. XRD spectra of all three AlN powders. Spectra from top to bottom: Atofina AlN, Stark AT, and AlN Stark C.

4.2 Composite Characterization

The densities of the hot pressed disks were determined by the Archimedes method. All samples were densified to over 98% theoretical density. The densities are tabulated in table 1.

Table 1. Densities of the TiB₂-AlN composites.

Vol% TiB ₂ – Vol% AlN (AlN type)	Density (g/cm ³)	Theoretical Density (%)
30–70 (Atofina)	3.61	99.18
30–70 (Stark C)	3.57	98.08
50–50 (Atofina)	3.84	98.71
50–50 (Stark C)	3.84	98.71
50–50 (Stark AT)	3.86	99.23
70–30 (Atofina)	4.06	98.07
70–30 (Stark AT)	4.08	98.55

The microstructures of the hot pressed composites were examined by SEM. SEM images of 30-70 TiB₂-AlN, 50-50 TiB₂-AlN, and 70-30 TiB₂-AlN (all samples with the Atofina AlN) are shown in figure 4. The images of the microstructures show some of the TiB₂ grains are elongated, and have faceted interfaces. The grain pull-outs are due to the polishing, which does

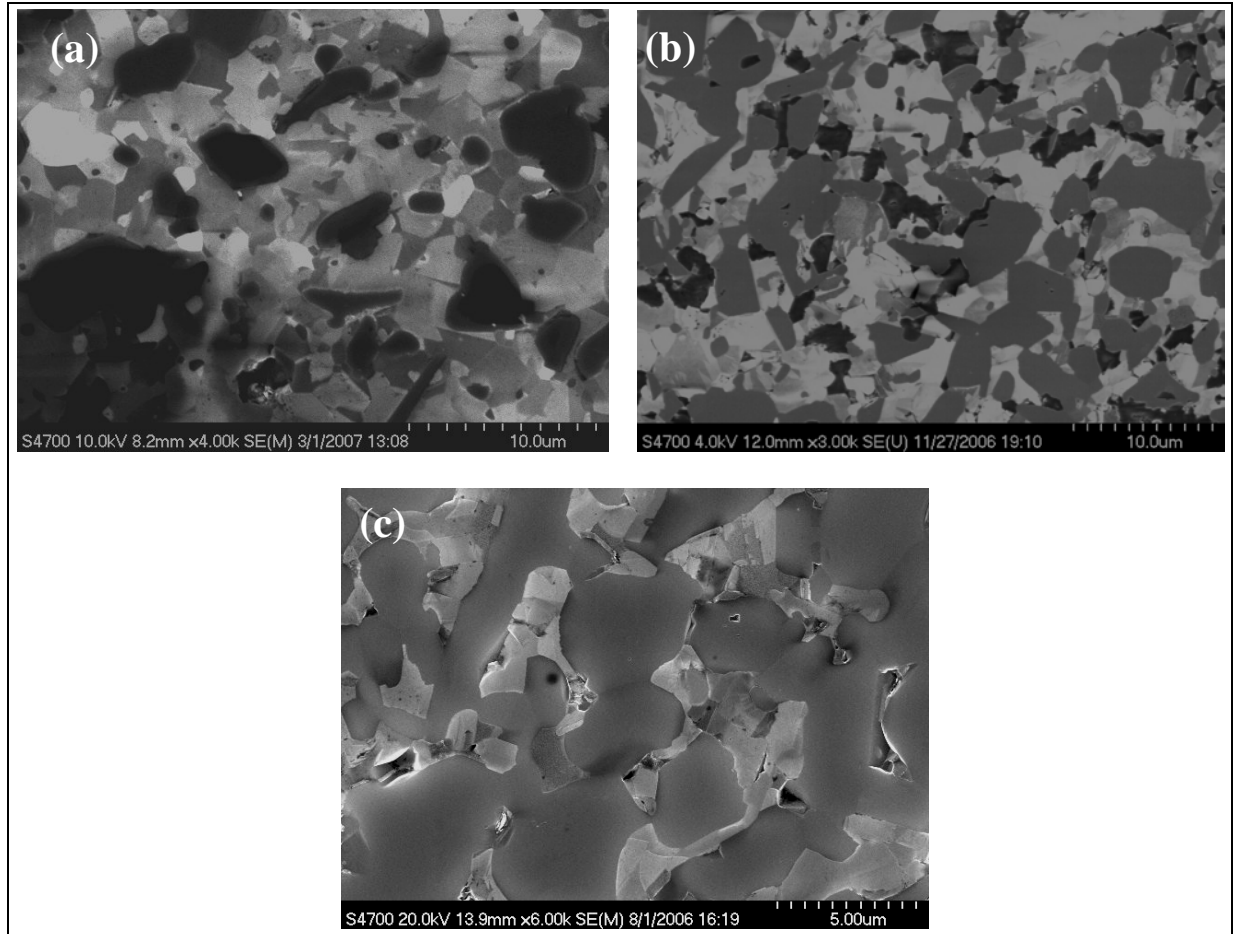


Figure 4. SEM images of (a) 30-70 TiB_2 -AlN, (b) 50-50 TiB_2 -AlN, and (c) 70-30 TiB_2 -AlN.

not indicate high porosity. EDS analysis of the grains indicate that the darkest areas are made up of primarily Al, with Si, O, N, and C. The Si and C are due to contamination possibly acquired during the processing steps. The medium gray grains were determined to be TiB_2 , the light gray grains were determined to be AlN, and the lightest colored grains appear to be Al_2O_3 . The existence of Al_2O_3 is believed to be from the Al_2O_3 milling balls used in the ball milling step.

In addition to characterization of the microstructure by SEM, EDS and EBSD scans were conducted on 50-50 TiB_2 -AlN (with the Atofina AlN) by Dr. Bassem El-Dasher of Lawrence Livermore National Laboratory. Due to the charging effects caused by the AlN grains, during the initial phase identification, the phases of 3% of the grains were inaccurately identified. However by applying the EDS scan map's phase identification of the same sample area, the incorrectly identified phases and indexes were manually corrected in the EBSD dataset. Figure 5 shows the initial phase identification, EDS phase identification, and the corrected EBSD inverse pole figure map. The different colors indicate the different surface normal orientations based on the standard stereographic triangle color key. From looking at the phase maps, it is clear that some agglomeration or clustering of grains of similar phases exists for both TiB_2 and AlN.

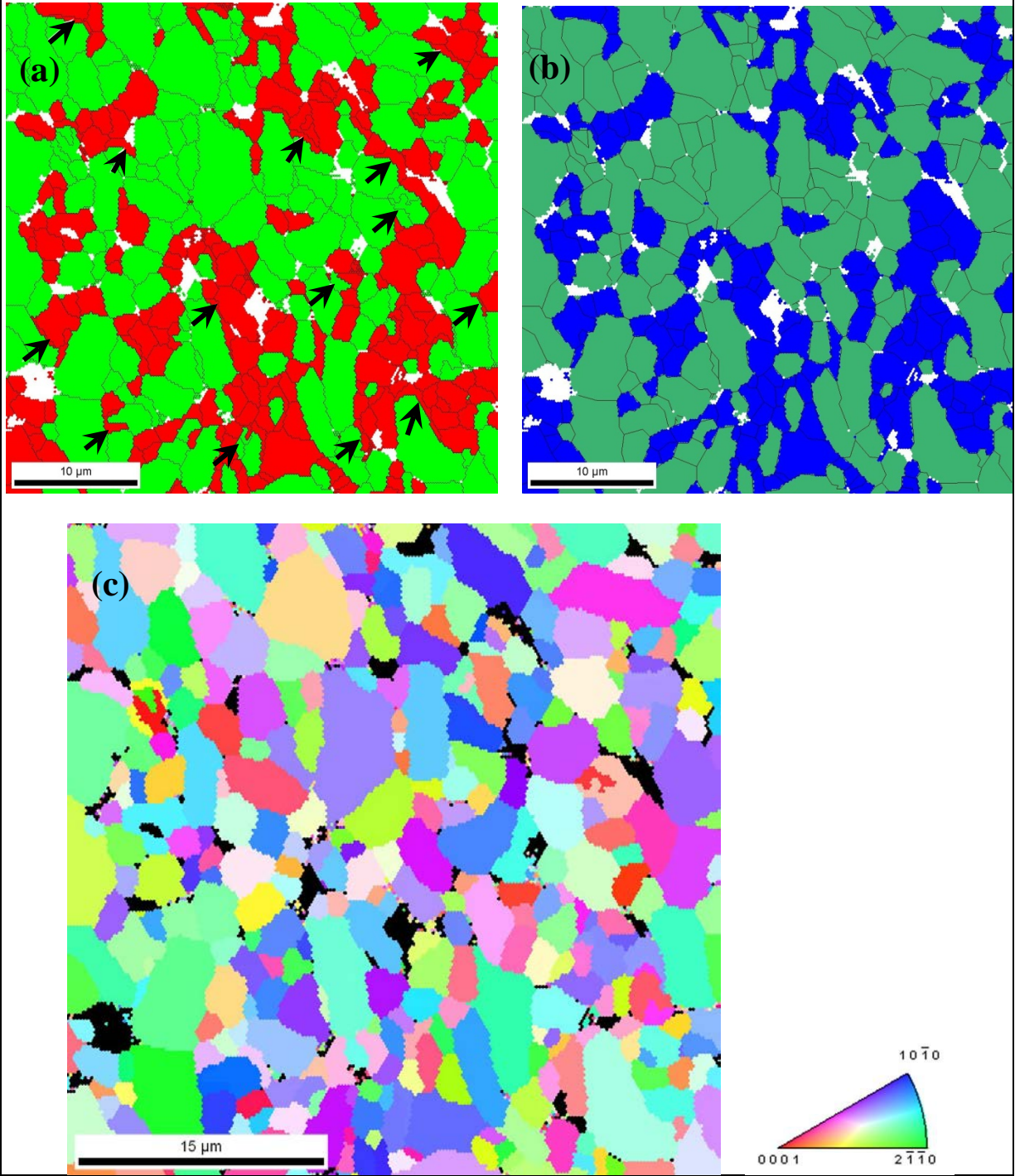


Figure 5. (a) Phase ID map of 50-50 TiB₂-AlN (with the Atofina AlN) before EDS aided correction. Arrows point to grains with erroneously identified phases. White areas are pores or voids where grains were pulled out during the polishing step. Green grains are TiB₂ and red grains are AlN. (b) Corrected phase map where green grains are TiB₂ and blue grains are AlN. (c) EBSD inverse pole figure map of the same area. The standard stereographic triangle key indicates the orientation corresponding to the grain color.

Over 97% of the number fractions of grain boundaries within each phase and also between phases were determined to be high-angle grain boundaries with misorientations greater than 15° . Less than 3% of the number fractions of grain boundaries for each phase and for interphase boundaries were low angle grain boundaries (0° to 15° misorientation).

It is worth noting that, in the composite, the TiB_2 did not appear to show any texturing, but pure TiB_2 shows some texturing based on the hot-pressing direction (see figure 6). EBSD scans on pure AlN showed random orientation distribution, as with the AlN phase in the composite (see figure 7). The number fraction of misorientation angles can show the amount of texturing, or deviation from a random misorientation distribution. Figure 8 shows the comparison of the number fraction the TiB_2 misorientation angles of the two surfaces as well as those of AlN misorientation angles compared to the random case. The AlN follows the random distribution except at the misorientation angles 30° , 64° , and 90° . These are most likely low-energy boundaries, and were more frequently observed than random. The misorientations in axis-angle notations were 30° about (10-10), 64° about (10-10), 90° about (10-10), and 90° about $(-12-10)$.

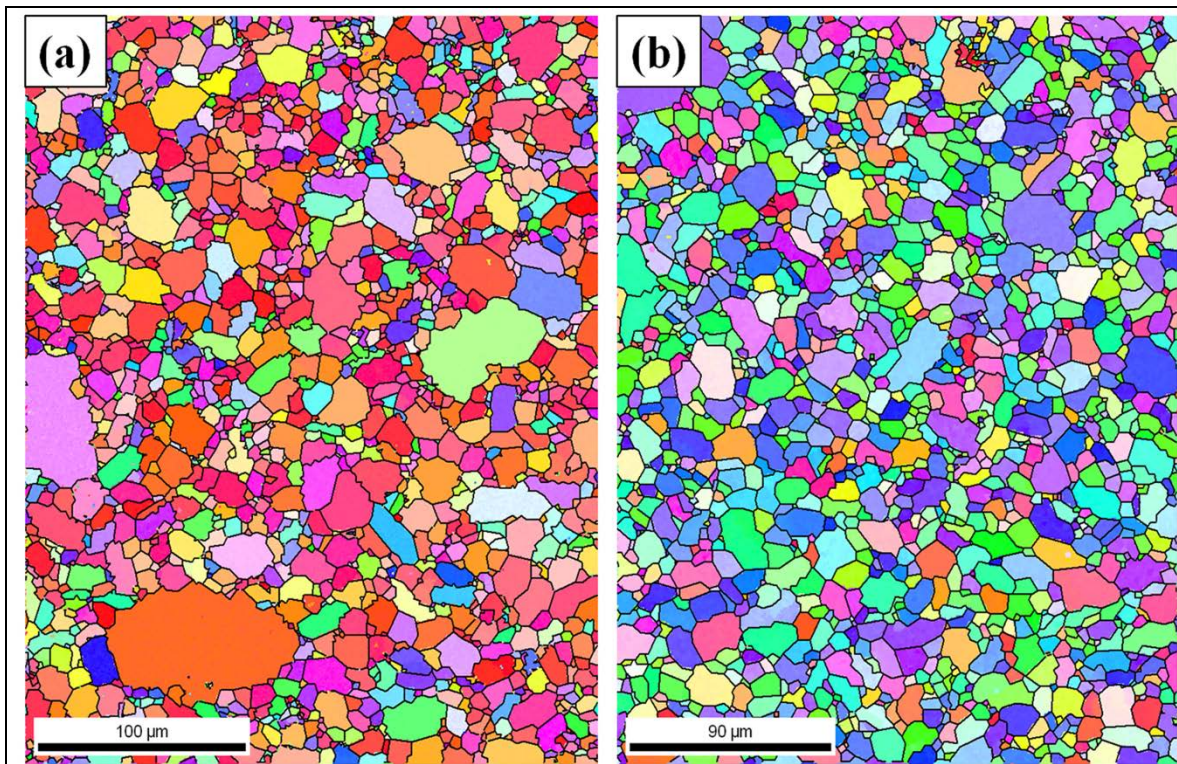


Figure 6. (a) Inverse pole figure map to the surface parallel to hot-pressing direction and (b) surface perpendicular to the hot-pressing direction.

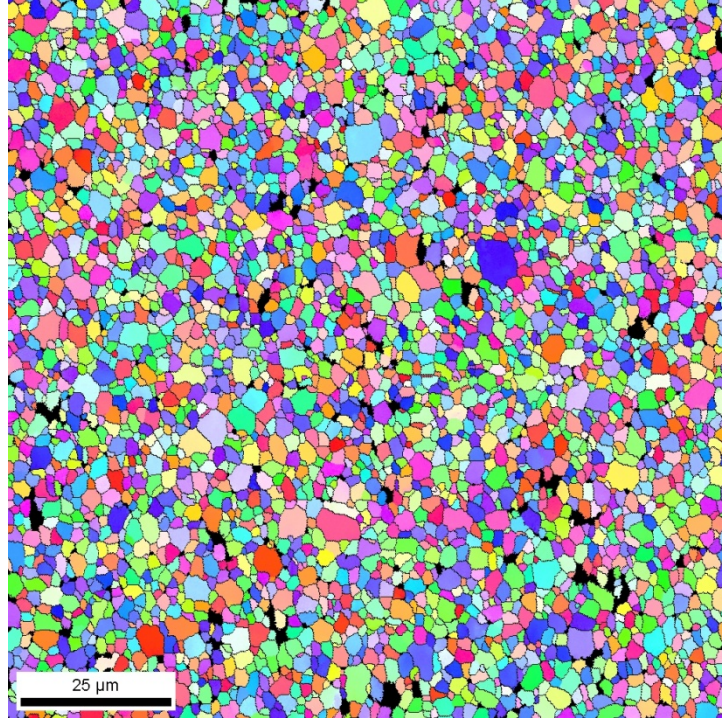


Figure 7. Inverse pole figure map of AlN.

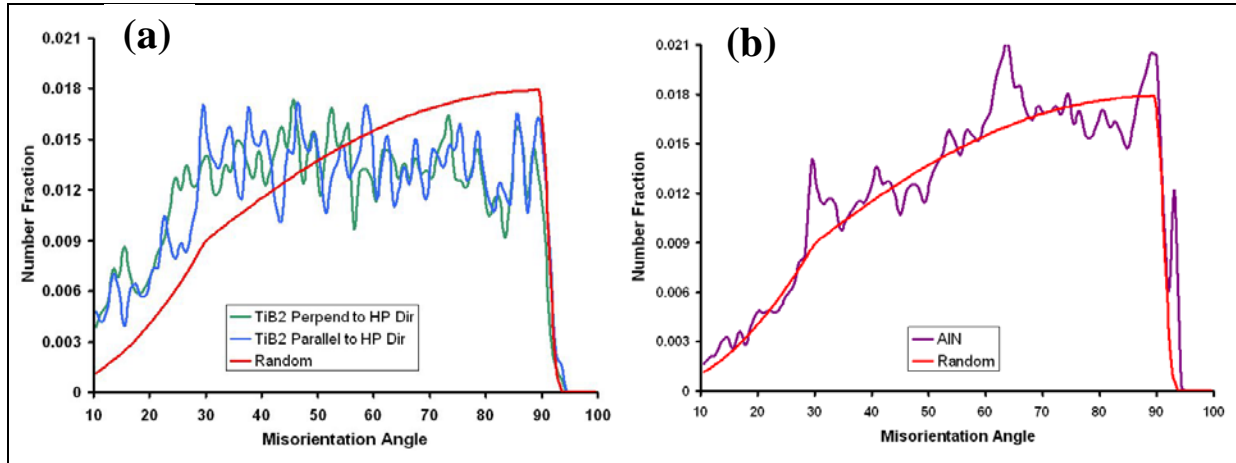


Figure 8. Number fraction of misorientation angles (a) for TiB₂ surfaces perpendicular to the hot-pressing direction and TB₂ surfaces parallel to the hot-pressing direction compared to a random, nontextured case, and (b) for AlN surfaces compared to random.

4.3 Mechanical Property Characterization

The flexural strength and Weibull modulus determined from the bend bars are tabulated in table 2. Thirty “B”-type bend bars were tested by four-point bend test per composition. Examples of the fracture surfaces are shown in figure 9. In some cases the flaw, such as cluster of AlN grains, was easily determined. However, in other cases, even by tracing the hackle lines to the mirror region, the flaws were not clear. As expected, the bend bars with obvious flaws had lower breaking loads and lower flexural strength. The mode of failure was both transgranular and intergranular fracture, and depended on the sample. The standard deviation and the Weibull modulus results indicate that the 50-50 TiB₂-AlN with the Atofina AlN powder had the most consistent strength and the least sample variability. The general trend of higher flexure strength with increase in TiB₂ content was also observed. A similar trend was observed for Knoop hardness, elastic modulus, shear modulus, and density. Table 3 lists the Knoop hardness values for the surfaces perpendicular and parallel to the hot-pressing direction. No hardness differences were detected based on the hot-pressing direction. Table 4 shows the modulus values and Poisson’s ratio measured by ultrasonic velocity tests. The modulus and Poisson’s Ratio results show that the TiB₂-AlN composites, especially the higher TiB₂ content compositions, are just as inelastic, or stiff as B₄C (which has elastic modulus of 445 GPa, shear modulus of 186 GPa, and Poisson’s ratio of 0.19 [25]), and are similarly resistant to shear forces. Likewise the Poisson’s Ratio indicates the TiB₂-AlN composites show little lateral expansion/compression when compressed/extended, like that of B₄C. Some of this trend for composite strength and modulus can be explained by the rule of mixtures (ROM), though one can argue that neither Reuss’ model nor Voigt’s model of ROM can be applied to modulus predictions in multiphase composites since the stresses (equal for Reuss ROM) and strains (equal for Voigt ROM) are not equal in each phase.

Table 2. Flexural strengths and Weibull modulus values.

Vol% TiB ₂ – Vol% AlN (AlN type)	Flexure Strength (MPa)	Standard Deviation (MPa)	Weibull Modulus
30–70 (Atofina)	501.3	46.3	15.74
50–50 (Atofina)	498.6	18.4	38.53
50–50 (Stark C)	527.4	54.8	16.72
50–50 (Stark AT)	432.9	28.4	20.84
70–30 (Atofina)	556.5	59.5	12.20
100% AlN	358.7	39.9	15.58
100% TiB ₂	366.2	36.9	15.33

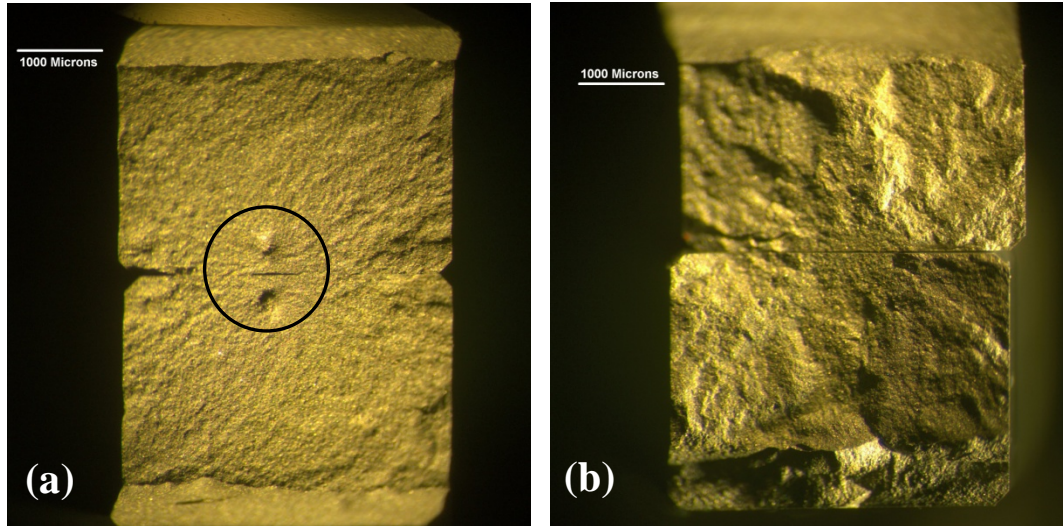


Figure 9. Example of (a) 30-70 TiB₂-AlN (with Atofina AlN) bend-bar fracture surface with grain cluster flaw circled (flexural strength = 338.4 MPa) and (b) 50-50 TiB₂-AlN (with Starck C AlN) bend-bar fracture surface with undetermined flaw (flexural strength = 576.7 MPa).

Table 3. Knoop hardness values for surfaces perpendicular to the hot-pressing direction and parallel to the hot-pressing direction.

Vol% TiB ₂ – Vol% AlN (AlN type)	Perpendicular Hardness (GPa)	Standard Deviation (GPa)	Parallel Hardness (GPa)	Standard Deviation (GPa)
30–70 (Atofina)	11.8	0.4	12.0	0.3
50–50 (Atofina)	12.7	0.2	13.2	0.5
5 –50 (Stark C)	14.2	0.3	13.6	0.4
50–50 (Stark AT)	13.6	0.5	13.5	0.5
70–30 (Atofina)	15.2	0.4	15.7	0.5

Table 4. Elastic modulus, shear modulus, and Poisson's ratio for some of the composites.

Vol% TiB ₂ – Vol% AlN (AlN type)	Elastic Modulus (GPa)	Shear Modulus (GPa)	Poisson's Ratio
30–70 (Atofina)	373	154	0.21
50–50 (Atofina)	407	174	0.17
50–50 (Stark AT)	407	174	0.17
70–30 (Atofina)	445	189	0.17

The fracture toughness for the 50-vol% compositions was measured with the single edge precracked beam method. The two fine-grained AlN samples had similar toughness values, but significantly higher toughness was observed in the sample with the coarse-grained AlN (Stark AT). The toughness values and the standard deviation are shown in table 5.

Table 5. Fracture toughness values.

Vol% TiB ₂ – Vol% AlN (AlN type)	Fracture Toughness (MPa√m)	Standard Deviation (MPa√m)
50–50 (Atofina)	5.6	0.3
50–50 (Stark C)	5.2	0.4
50–50 (Stark AT)	7.0	0.1

4.4 Residual Stress Characterization

Raman spectra was acquired and used to determine the residual stress of AlN in the composite. Pure AlN Raman spectra and the spectra of 50-50 TiB₂-AlN (in this case, Atofina AlN) was experimentally obtained. Compared to that of pure AlN, which had an E₂ (high) phonon frequency of 656.60 cm⁻¹, the AlN in the composite recorded an E₂ (high) phonon frequency of 658.29 cm⁻¹, indicating a shift of 1.69 cm⁻¹. Since a positive cm⁻¹ shift indicates a 0.2 GPa compression, the AlN in the composite was calculated to be in 0.34 GPa of compression. Since AlN undergoes a brittle to ductile transition at the confining pressure of 0.55 GPa (8, 9) this level of pre-stress could lead to the AlN experiencing a ductile to brittle transition earlier in the ballistic event. This could lead to enhanced ballistic performance. No microstructural evidence was found to either support or refute this supposition. This is not surprising given the difficulty in analyzing post impact ceramic failure mechanisms.

4.5 Phase Diagram of TiB₂-AlN

To determine the thermodynamic phase calculations for the TiB₂-AlN system, it was necessary to first conduct calculation of the phase diagrams of the possibly binary phase systems. Using the thermodynamic database for the Ti-Al-B-N system, all binary phase diagrams were created. Using the binary systems, the ternary systems were also recreated with numerous isotherms. Figure 10 shows the possible phases in the binary and ternary systems. The quaternary system was calculated while taking into the account the known stable phases determined from the binary and ternary systems. Figure 11 (a) shows the quaternary isothermal section at constant Ti atomic content, X (Ti) =0.1, at T = 1573 K and (b) shows the quaternary isothermal section at constant B atomic content, X (B) =0.1, at T = 1573 K. It was determined from the phase diagrams that TiB₂-AlN is a stable line composition in the ternary and quaternary systems, indicating no reactions below the melting point of AlN at 2700 K. However any small deviation from this composition line (outside of the red circled point in figure 11) will result in formation of different phases and compositions, such as BN and TiN. If impurities are introduced to this composition, the possible phases and compositions will increase. Impurities or a slight deviation from the TiB₂-AlN line composition is believed to be the case, since unexpected solid phases were observed, as seen in figure 12. The details of each of the binary phases and ternary phases, and other observations can be found in the final report (21).

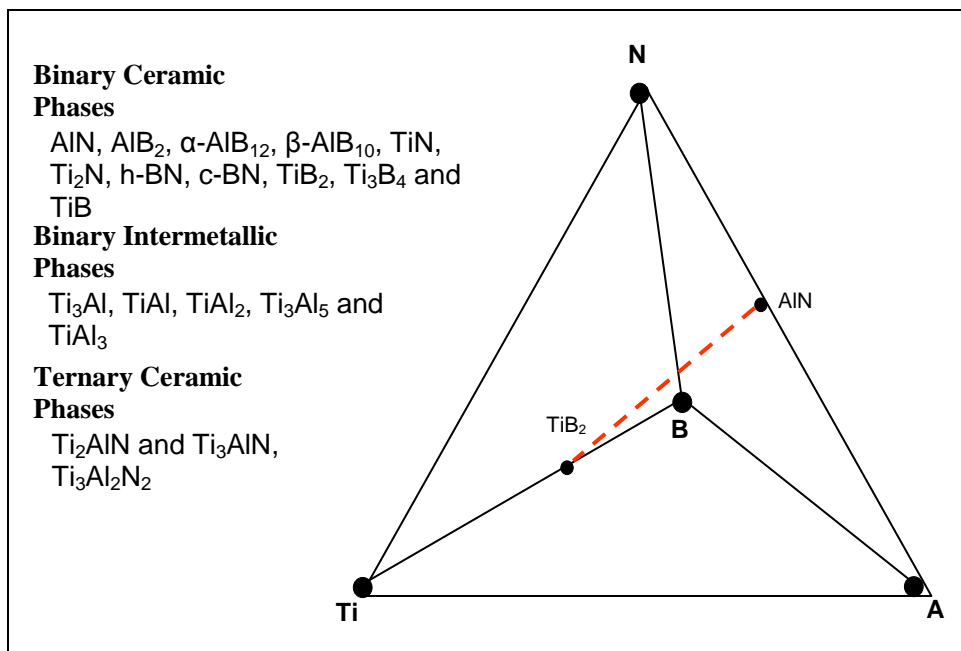


Figure 10. Possible phases in the binary and ternary Ti-B-Al-N system.

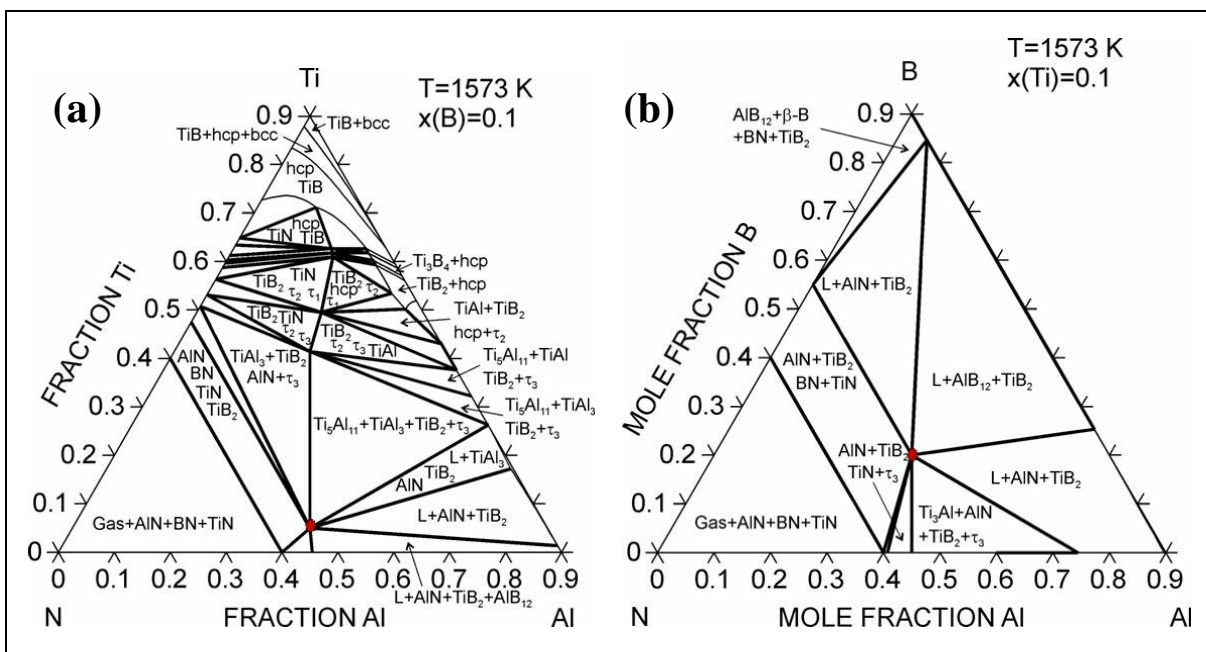


Figure 11. (a) Quaternary isothermal section at constant Ti atomic content, $X(\text{Ti}) = 0.1$, at $T = 1573 \text{ K}$ and (b) Quaternary isothermal section at constant B atomic content, $X(\text{B}) = 0.1$, at $T = 1573 \text{ K}$.

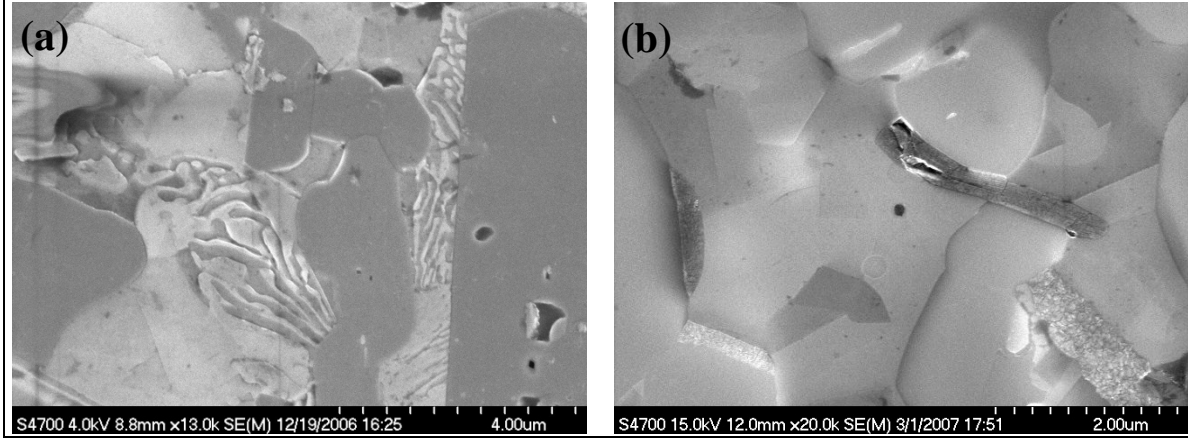


Figure 12. (a) SEM image of 50-vol% TiB_2 / 50-vol% AlN (with Atofina AlN) showing what is believed to be AlN and γ -AlON decomposed eutectoid regions and (b) SEM image of 70-vol% TiB_2 / 30-vol% AlN (with Atofina AlN) showing possibly TiN impurities at the grain boundaries.

4.6 Mass Efficiency Results

The DOP ballistic test was conducted on pure TiB_2 , pure AlN, on one composition of 30-70 TiB_2 -AlN and 70-30 TiB_2 -AlN, and three compositions of 50-50 TiB_2 -AlN (with all three types of AlN). From the DOP tests, mass efficiency (E_m) values were calculated by the relation

$$E_m = \frac{\left(\text{Penetration}_{\text{RHAequivalent}} - \text{Penetration}_{\text{CeramicTile}} \right) \cdot \rho_{\text{Steel}}}{\rho_{\text{Ceramic}} \cdot \text{Thickness}_{\text{CeramicTile}}}, \quad (4)$$

where ρ is density in g/cm^3 .

Figure 13 is a plot of the E_m data with respect to the velocity of the tungsten heave alloy penetrator. The error bars are the average absolute deviation. Although DOP tests were not conducted on all the composite varieties, from this plot, several correlations can be formed. From inspecting the pure TiB_2 , pure AlN, and 50-50 TiB_2 -AlN (with Atofina AlN) data, E_m decreases with velocity. The composites, regardless of the ratio of TiB_2 to AlN, either performed comparably well, as with the 30-70 TiB_2 -AlN (with Stark C AlN), or better than the pure components. And even though 50-50 TiB_2 -AlN (with Stark AT AlN) has the more of the ductile AlN than 70-30 TiB_2 -AlN (with Stark AT AlN), the E_m results are similar. Comparing 50-50 TiB_2 -AlN (with Stark AT AlN) with the 50-50 TiB_2 -AlN (with Stark C AlN), the composite with the coarse-grain AlN (Stark AT) performed better. Comparison with the 50-50 TiB_2 -AlN (with Atofina AlN) could not be made due to the large range of E_m values, which could be attributed to the hot-pressing repeatability issues or target processing.

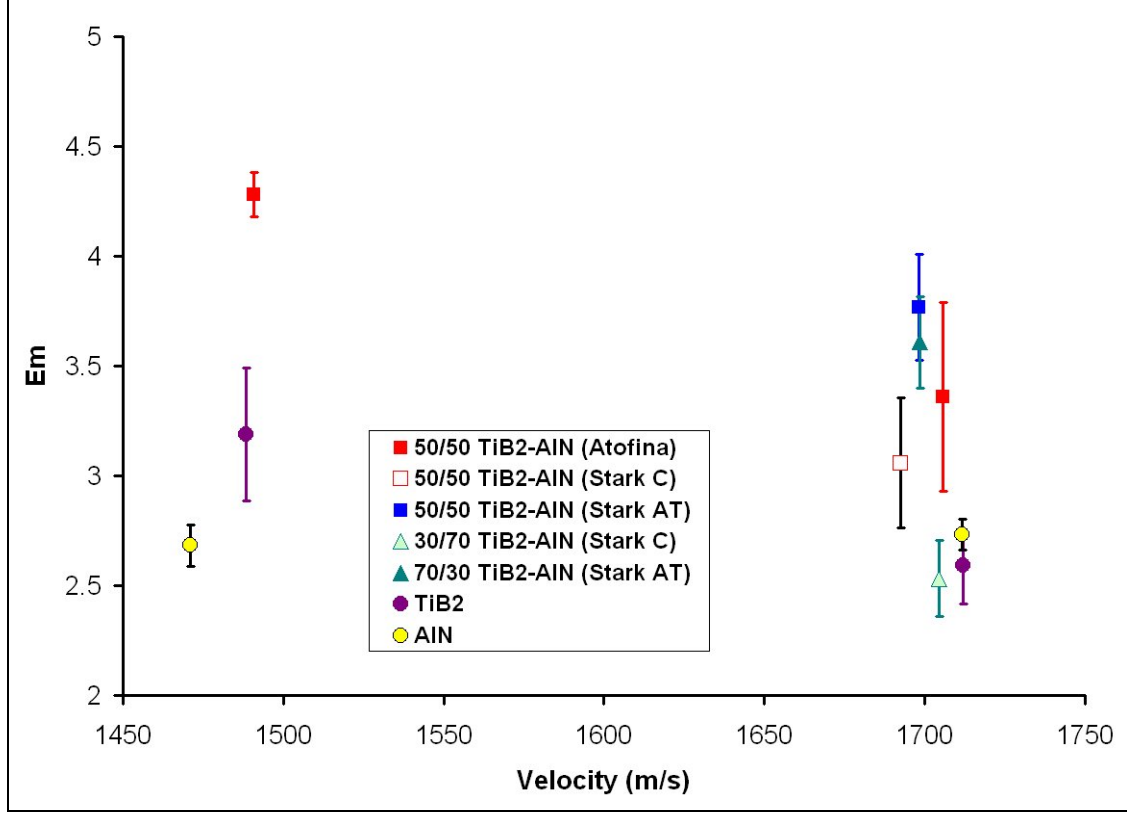


Figure 13. E_m vs. velocity for some of the composites and pure TiB₂ and pure AlN.

5. Discussion

The reason behind the better performance of the 50-50 TiB₂-AlN with the coarse-grained Stark AT compared to the other composites was examined. The hypothesis is that the Stark AT AlN contributed to increase in toughness. The predicted fracture toughness was 3.88 MPa√m; however, the measured fracture toughness for the 50-50 TiB₂-AlN with the coarse-grained Stark AT was 7.0 MPa√m. The mechanism of the increase in toughness is believed to be a combination of microcrack toughening and crack deflection or crack bridging due to residual stress contributions.

For microcracks to increase toughness (26), the grain size must be less than d_c , but larger than r_c . The relations for d_c and r_c are

$$d_c = \left(\frac{K_c}{\sigma_R} \right)^2 \quad (5)$$

and

$$r_c \cong d \left\{ \frac{0.23}{\left[1 - \left(\frac{d}{d_c} \right)^{1/2} \right]} \right\}, \quad (6)$$

where K_c is the fracture toughness, σ_R is the residual stress, and d is the grain size. For 50-50 TiB₂-AlN, the d_c for AlN was calculated to be 8 μm and r_c was calculated to be 0.3 μm . Since the Stark AT AlN grain diameters fall within the microcrack toughening range, it is possible for the composite's toughening to increase by microcracks.

Crack bridging by elongated second phase grains are known to increase toughening (27). However crack bridging can also occur due to residual stress effects. The compression stresses due to the residual stress causes cracks to seek lower stressed paths (28). The grain boundaries of interphase boundaries with low fracture energies can debond and increase the toughness. Some of the coarse-grained AlN by Stark showed elongated grains, but a definitive crack bridging event was not readily observed. However, the fracture surfaces of the bend bars show a clear difference between those of the 50-50 TiB₂-AlN with the coarse-grained Stark AT AlN and those with the Atofina AlN. Figure 14 shows the difference in the fracture surfaces near the fracture origin. While the composite with the Stark AT AlN shows intergranular fracture, the composite with the Atofina AlN shows transgranular fracture.

Assuming the toughness increase was due to microcracks and crack deflection/bridging, the following equations were used to calculate the increase. The increase in toughness due to microcracks (29) is shown as

$$\Delta G_c = \frac{\beta G_{co} (\Delta\alpha) (\Delta T) E}{\sigma_R}, \quad (7)$$

where β is a coefficient, typically 0.1, G_{co} is the toughness of the material without microcracks, $\Delta\alpha$ is the difference in thermal expansion coefficients, ΔT is the difference in temperature the material experiences, and E is the Young's modulus. The G_c (or G_{co} in this case) for plane stress conditions, can be determined by the relation,

$$G_c = \frac{K_c^2}{E}. \quad (8)$$

The increase in toughness due to crack bridging, or work required to pull-out grains confined with residual stresses is

$$\Delta G_c \cong \frac{1}{8} \mu \sigma_R V_f d, \quad (9)$$

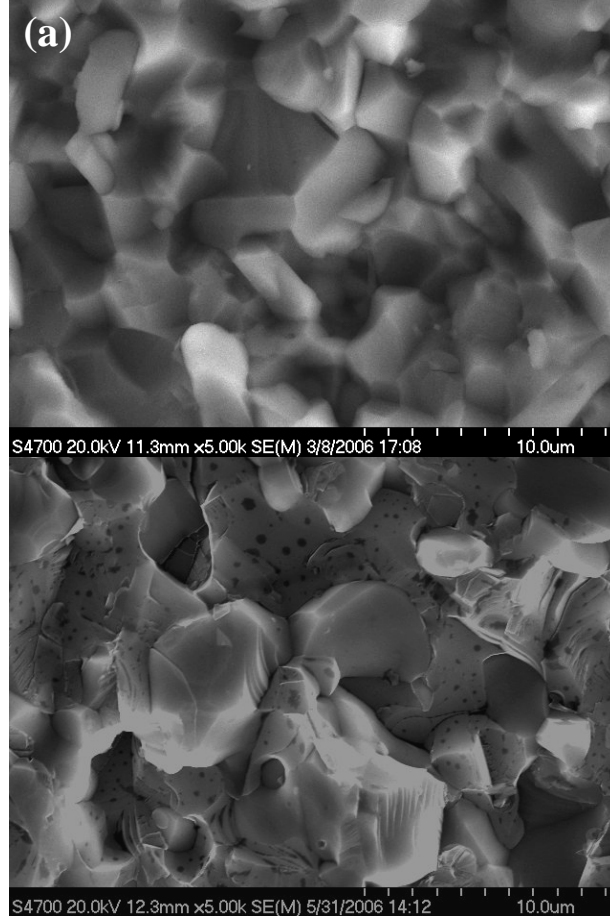


Figure 14. (a) Intergranular fracture surface of 50-50 TiB_2 -AlN with the coarse-grained Stark AT AlN and (b) transgranular fracture surface of 50-50 TiB_2 -AlN with the fine-grained Atophina AlN showing cleavage facets.

where μ is the coefficient of friction, and V_f is the volume fraction of grains subject to crack bridging. Using the theoretical values, G_{co} was calculated to be 33.7 J/m^2 . For the increase in toughness due to microcracks, using the difference in the coefficient of thermal expansion between TiB_2 and AlN, and the experimental values of Young's modulus of the composite and of the residual stress, $\Delta G_{c\text{-microcrack}}$ was calculated to be 30.9 J/m^2 . Using μ for AlN of 0.2, determined by Mosina et al. (29), AlN V_f of 0.43 and d of $2.51 \text{ }\mu\text{m}$ measured from SEM images, the increase in toughness from crack bridging, $\Delta G_{c\text{-crack bridging}}$ was calculated to be 9.2 J/m^2 . From the combined ΔG_c , the increase the fracture toughness was determined to be $4.0 \text{ MPa}\sqrt{\text{m}}$. Adding this to the initially predicted fracture toughness of $3.88 \text{ MPa}\sqrt{\text{m}}$, the total fracture toughness is $7.88 \text{ MPa}\sqrt{\text{m}}$, a comparable value to the $7.0 \text{ MPa}\sqrt{\text{m}}$ measured experimentally. It is possible that the increase in the fracture toughness is the cause of the synergistic effect observed for the flexural strengths of the composites as well.

6. Conclusions

To improve ceramic armor material performance, composites with TiB_2 and AlN of varying compositions were consolidated by hot pressing. The composites were made with three types of AlN, and were of the composition 30-70 TiB_2 -AlN, 50-50 TiB_2 -AlN, and 70-30 TiB_2 -AlN. The characterization included powder and composite morphology and atomic content, impurity identification, density, crystallographic orientation, residual stress, and mechanical property evaluation. Theoretical phase calculations and analysis were conducted, as well as ballistic performance evaluation by DOP tests.

The results indicate that this composite is a complex material to properly characterize for armor applications, due to impurity effects on phase formation and grain size effects compounded with residual stress on the fracture mechanisms. However, it was determined that the composite with the highest fracture toughness resulted in the best mass efficiency values. The influence of fracture toughness on ballistic performance (30) has been discussed and evaluated for many years. Hence, the increase in fracture toughness improving the mass efficiency (as well as the flexural strength) is a plausible correlation and explanation of the synergistic results. For the TiB_2 -AlN composite, the increase in fracture toughness is believed to be due to microcrack formation and residual stress causing crack bridging. More experiments with larger and elongated AlN grains are necessary to definitively conclude the impact of the grain microstructure on the ballistic performance.

7. References

1. Chin, E. Army Focused Research Team on Functionally Graded Armor Composites. *Mater. Sci. Eng. A* **1999**, 259, 155–161.
2. Pettersson A.; Magnusson, P.; Lundberg, P.; Nygren, M. Titanium-Titanium Diboride Composite as Part of a Gradient Armour Material. *Int. J. Imp Eng.* **2005**, 32, 387–399.
3. Munro, R. G. Material Properties of Titanium Diboride. *J. Res. Natl. Inst. Stand. Technol.* **2000**, 105, 709–720.
4. Han, Y.; Dai, Y.; Shu, D.; Wang, J.; Sun, B. First-Principles Study of TiB₂ (0001) Surfaces. *J. Phys.: Condens. Matter* **2006**, 18, 4197–4205.
5. Vajeeston, P.; Ravindran, P.; Ravi, C.; Asokamani, R. Electronic Structure, Bonding, and Ground-State Properties of AlB₂-Type Transition-Metal Diborides. *Phys. Rev. B* **2001**, 63, 045115.
6. Lonnberg, B. Thermal Expansion Studies on the Group IV-VII Transition Metal Diborides. *J. Less-Common Met.* **1988**, 141, 145–156.
7. Seifert, A.; Berger, A.; Muller, W. F. TEM of Dislocation in AlN. *J. Am. Ceram. Soc.* **1992**, 75 (4), 873–877.
8. Heard, H. C.; Cline, C. F. Mechanical Behavior of Polycrystalline BeO, Al₂O₃ and AlN at High Pressure. *J. Mat. Sci.* **1980**, 15, 1889–1897.
9. Chen, W.; Ravichandran, G. Failure Mode Transition in Ceramics Under Dynamic Multiaxial Compression. *Int. J. Fracture* **2000**, 101, 141–159.
10. Yim, W. M.; Paff, R. J. Thermal Expansion of AlN, Sapphire, and Silicon. *J. Appl. Phys.* **1974**, 45 (3), 1456–1457.
11. Zhang, G. J.; Jin, Z. Z. Reactive Synthesis of AlN/TiB₂ Composite. *Ceram. Int.* **1996**, 22, 143–147.
12. Xu, G-F.; Carmel, Y.; Olorunyolemi, T.; Lloyd, I. K.; Wilson, O. C. Microwave Sintering and Properties of AlN/TiB₂ Composites. *J. Mater. Res.* **2003**, 18 (1), 66–76.
13. Kim, H-J.; Choi, H-J.; Lee, J-G. Mechanical Synthesis and Pressureless Sintering of TiB₂-AlN Composites. *J. Amer. Ceram. Soc.* **2002**, 85 (4), 1022–1024.
14. Li, L-H.; Kim, H-E.; Kang, E. S. Sintering and Mechanical Properties of Titanium Diboride With Aluminum Nitride as a Sintering Aid. *J. Eur. Ceram. Soc.* **2002**, 22, 973–977.

15. Zdaniewski, W. A. Stereoscopic Fractography of Crack Propagation Phenomena in a TiB₂-AlN Composite. *J. Amer. Ceram. Soc.* **1989**, 72 (1), 116–121.
16. Zdaniewski, W. A. Fracture of Polycrystalline TiB₂-AlN Composites in Various Environments. *Acta Metall.* **1989**, 37 (9), 2313–2320.
17. ASTM C 1161-02c. Standard Test Method for Flexural Strength of Advanced Ceramics at Ambient Temperature. *Annu. Book ASTM Stand.* **2002**, Vol. 15.01.
18. ASTM C 1421-10. Standard Test Methods for Determination of Fracture Toughness of Advanced Ceramics at Ambient Temperature. *Annu. Book ASTM Stand.* **2002**, Vol. 15.01.
19. ASTM E 494. Standard Practice for Measuring Ultrasonic Velocity in Materials. *Annu. Book ASTM Stand.* **2000**, Vol. 3.03.
20. Kuball, M.; Hayes, J. M.; Prins, A. D.; van Uden, N. W. A.; Dunstan, D. J.; Shi, Y.; Edgar, J. H. Raman Scattering Studies on Single-Crystalline Bulk AlN Under High Pressures. *Appl. Phys. Lett.* **2001**, 78 (6), 724–726.
21. Fabrichnaya, O.; Seifert, H. J. *Phase Diagram Development for TiB₂-AlN and B-C Systems*; TCN 05133/D.O.0663; Final Report for Army Research Laboratory, Contract No. DAAD19-02-D-0001, 2007.
22. Zhang H.; Li, F. Preparation and Microstructure Evolution of Diboride Ultrafine Powder by Sol-Gel and Microwave Carbothermal Reduction Method. *J. Sol-Gel Technol.* **2008**, 45, 205–211.
23. Subramanian, C.; Murthy, T. S. R. Ch.; Suri, A. K. Synthesis and Consolidation of Titanium Diboride. *Int. J. Refract Met Hard Mater.* **2007**, 25, 345–350.
24. Matsudaira, T.; Itoh, H.; Naka, S.; Hamamoto, H.; Obayashi, M. Synthesis of TiB₂ Powder from a Mixture of TiN and Amorphous Boron. *J. Mater Sci.* **1988**, 23, 288–292.
25. Shaffer, P. T. B. Engineering Properties of Carbides. *Engineered Materials Handbook*; Vol. 4; Schneider, S. J., Jr., Ed.; ASM International, 1991; pp. 804–811.
26. Courtney, T. H. *Mechanical Behavior of Materials*; 2nd ed.; McGraw-Hill: New York, 2000; p 464–471.
27. Becher, P. F. Microstructural Design of Toughened Ceramics. *J. Am. Ceram. Soc.* **1991**, 74 (2), 255–269.
28. Evans, A. G. Perspective on the Development of High-Toughness Ceramics. *J. Am. Ceram. Soc.* **1990**, 73 (2), 187–206.

29. Mosina, T. V.; Panasyuk, A. D.; Yuka, A. I.; Grigor'ev, O. N. Friction Properties of Composite of the System TiN-AlN. I. Effect of Structure and Phase Composition on Friction and Wear of Materials of the System TiN-AlN. *Powder Metall. Met. Ceram.* **1999**, 38 (9–10), 517–520.
30. Karandikar, P. G.; Evans, G.; Wong, S.; Aghajanian, M. K. A Review of Ceramics for Armor Applications. In *Advances in Ceramic Armor IV: Ceramic Engineering and Science Proceedings*, Vol. 29, Issue 6. Prokurat Franks, ed., John Wiley and Sons, Inc.: Hoboken, NJ, 2008; p 163–178.

NO. OF
COPIES ORGANIZATION

1 DEFENSE TECHNICAL
(PDF) INFORMATION CTR
DTIC OCA

1 DIRECTOR
(PDF) US ARMY RESEARCH LAB
IMAL HRA

1 DIRECTOR
(PDF) US ARMY RESEARCH LAB
RDRL CIO LL

1 GOVT PRINTG OFC
(PDF) A MALHOTRA

ABERDEEN PROVING GROUND

1 DIR USARL
(PDF) RDRL WMM E
T SANO

INTENTIONALLY LEFT BLANK.